Published in final edited form as:

Nat Chem. 2019 June ; 11(6): 521–532. doi:10.1038/s41557-019-0261-6.

Diverse compounds from pleuromutilin lead to a thioredoxin inhibitor and inducer of ferroptosis

Evijola Llabani[1], **Robert W. Hicklin**[1], **Hyang Yeon Lee**[1], **Stephen E. Motika**[1], **Lisa A. Crawford**[2], **Eranthie Weerapana**[2], and **Paul J. Hergenrother**[1,*]

[1]Department of Chemistry, Roger Adams Laboratory, University of Illinois, 600 S. Mathews Ave., Urbana, IL, 61801

[2]Department of Chemistry, Boston College, Chestnut Hill, MA, 02467

Abstract

The chemical diversification of natural products provides a robust and general method for creation of stereochemically rich and structurally diverse small molecules. The resulting compounds have physicochemical traits different from those in most screening collections, and as such are an excellent source for biological discovery. Herein, we subject the diterpene natural product pleuromutilin to reaction sequences focused on creating ring system diversity in few synthetic steps. This effort resulted in a collection of compounds with previously unreported ring systems, providing a novel set of structurally diverse and highly complex compounds suitable for screening in a variety of different settings. Biological evaluation identified the novel compound ferroptocide, a small molecule that rapidly and robustly induces ferroptotic death of cancer cells. Target identification efforts and CRISPR knockout studies reveal that ferroptocide is an inhibitor of thioredoxin, a key component of the antioxidant system in the cell. Ferroptocide positively modulates the immune system in a murine model of breast cancer and will be a useful tool to study the utility of pro-ferroptotic agents for treatment of cancer.

Graphical Abstract

*Correspondence and requests for materials should be addressed to P.J.H. (hergenro@illinois.edu).

Author contributions

P.J.H., E.Ll. and R.W.H. conceived this study. R.W.H designed and synthesized all compounds. E.Ll. designed and performed all biological experiments and analyzed data. H.Y.L. performed the mouse model studies. S.E.M. synthesized the lead compound for the mouse model. L.A.C. and E.W. collected and analyzed the LC/LC–MS/MS data. P.J.H. supervised this research. P.J.H and E.LI. wrote this manuscript with the assistance of R.W.H. All authors have given their approval of the final version of the manuscript.

Competing interests

The University of Illinois has filed patents on some compounds described in this manuscript.

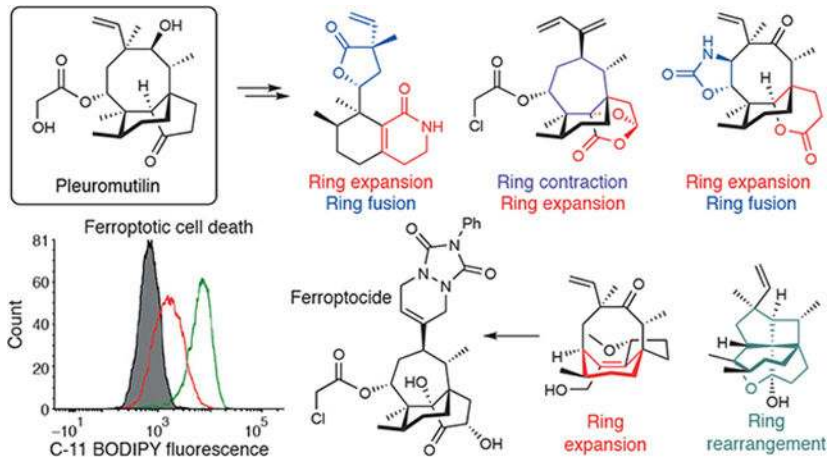

Structurally complex small molecules play an important role in probing biological systems and combating disease. Such compounds often contain dense polycyclic ring systems, multiple stereogenic centers, and spatially defined arrangements of functional groups. The complexity and three-dimensionality of these molecules allows for specific interactions with biological macromolecules and selective modulation of cellular pathways; such compounds are complimentary to those in large commercial screening collections that tend to have fewer stereogenic centers and more sp^2-hybridized carbons.[1,2]

Several strategies for the rapid and efficient synthesis of value-added complex compounds have been developed, including those that construct complex scaffolds from diverse collections of simple building blocks,[3,4] and those that begin with complexity and build in diversity.[5] For this later approach, natural products offer a rich and varied source of starting materials, and collections of compounds have been assembled using the Complexity-to-Diversity (CtD) strategy from the natural products adrenosterone,[6] gibberellic acid,[6] quinine,[6,7] abietic acid,[8] sinomenine,[9] lycorine,[10] yohimbine,[11] haemanthamine,[12] nitrogenous steroids of dutasteride and abiraterone acetate,[13] ilimaquinone,[14] and others. The resulting collections have been used to discover small molecules with anticancer and antimicrobial activities,[11,15] autophagy inhibitors,[16] and to identify predictive guidelines for broad-spectrum antibiotic discovery.[17]

The CtD strategy is applied herein to the natural product pleuromutilin (**P**, Fig. 1) with an emphasis on transforming the highly dense ring system of **P** into compounds with novel and complex ring architectures in short synthetic sequences. The resulting compounds were then evaluated for their ability to induce rapid death of cancer cells, with an eye toward the discovery of compounds with unusual modes of action. We now report the identification of **ferroptocide**, a novel compound that induces rapid ferroptotic death of cancer cells and inhibits thioredoxin; its mechanism of ferroptotic induction makes **ferroptocide** distinct from and complementary to existing ferroptosis inducers. Additionally, **ferroptocide** has immunostimulatory activity in a murine cancer model and thus will be an important tool for further investigating the potential of ferroptosis-inducing agents to act in concert with the immune system as an anticancer strategy.

Results and discussion

Diversifying Pleuromutilin

The diterpene natural product **P** is found in several species of fungi and is a potent inhibitor of the bacterial 50S ribosome.[18] **P** is composed of 5-, 6-, and 8-membered rings and contains eight contiguous stereogenic centers. Several semisynthetic derivatives of **P** are used to treat Gram-positive pathogens in humans (retapamulin) and in veterinary medicine (tiamulin, valnemulin),[18] and recently epi-mutilin derivatives have been developed as antibiotics with activity against some Gram-negative bacteria.[19–22] Investigation of the antibacterial activity of **P** and its derivatives has inspired several total synthesis efforts[20,21,23–25] that, combined with previous work on structure elucidation[26,27] and structure–activity relationship studies,[18,28,29] provide a wealth of synthetic information about the chemical reactivity of the pleuromutilin ring system. Structural transformations of the **P** ring system identified through these efforts afford several good starting points for novel diversification reactions. With the objective of harnessing the advantages of **P** as a starting material to construct a small set of highly complex and structurally diverse compounds, we set out to alter the ring systems of pleuromutilin through a series of ring contraction, expansion, cleavage, and fusion reactions (Fig. 1).

Treatment of pleuromutilin with phosphorus pentachloride results in activation of the secondary alcohol, carbocation rearrangement, and ring contraction to form known diene **P1**[26] (Fig. 1a) as a single diastereomer whose absolute configuration was confirmed by X-ray crystallography (Supplementary Table 1). **P1** is an outstanding starting point for the construction of novel compounds with unusual oxidation patterns and ring systems. For example, silylation of **P1** results in formation of the **P2** kinetic silyl enol ether. Subsequent Rubottom oxidation induces an alcohol-directed epoxidation on the less hindered face of the five-membered ring, yielding epoxide **P3** as a single diastereomer (Fig 1a). Desilylation of **P3** to **P4** (Fig. 1a) provides an α-hydroxy ketone, that upon exposure to lead tetraacetate produces a novel rearrangement yielding **P5**. This proceeds through oxidative cleavage of the less hindered C-C bond of the hydroxy ketone, resulting in an intermediate containing an aldehyde and ester. Hemiacetal formation between the tertiary alcohol and aldehyde, followed by subsequent lactonization efficiently installs two new stereocenters via diastereoselective oxidation and results in a ring rearrangement to form **P5**.

In addition to the direct formation of **P1** from pleuromutilin, the use of carbocation rearrangements is a useful strategy for inducing dramatic changes to the overlapping rings of pleuromutilin. In aiming to construct a subset of compounds in which the 6-membered ring was expanded, we identified alcohol **P6**, a common intermediate in the synthesis of pleuromutilin-derived antibiotics,[30,31] as a useful substrate (Fig. 1b). **P6** was generated via acid catalyzed isomerization and subsequent 1,5-hydride shift of pleuromutilin, as reported previously.[30] Treatment of **P6** with phosphorus pentachloride resulted in a novel expansion of the 6-membered ring and elimination to form a new scaffold, **P7**, as a single isomer. Further modification of **P7** was accomplished by diastereoselective epoxidation of the disubstituted olefin to afford novel scaffold **P8**. Elimination and epoxide opening of **P8** forms a new allylic alcohol **P9** (Fig. 1b).

Cleavage of the 8-membered ring of **P** has been reported to occur via a retro-Michael reaction.[24] Indeed, oxidation of the secondary alcohol of pleuromutilin affords a 1,5-diketone that after retro-Michael ring cleavage with potassium hydroxide, and oxidation of the resulting ketal with pyridinium chlorochromate provides known lactone **P10** (Fig. 1c).[24] Compound **P10** was then used to construct novel lactam **P12**, through ring expansion of the cyclopentanone ring of **P10** induced by oxime formation (**P11**) and Beckmann rearrangement initiated by cyanuric chloride (Fig. 1c).

Finally, ring fusion to the 8-membered ring of **P** was achieved by intramolecular C–H insertion of a primary carbamate (Fig. 1d). Inspired by previous work on C–H amidation of the epi-mutilin scaffold,[32] ring fusion precursor **P13** was synthesized by saponification of pleuromutilin followed by acylation and carbamylation (see Supplementary Scheme 4). Intramolecular C–H nitrene insertion was accomplished using modified silver-catalyzed methodology[32] to provide the novel ring system found in carbamate **P14**. Exposure of this product to alkaline autoxidation conditions[26] results in a formal ring expansion of the 5-membered ring via enolate formation, oxidative cleavage, hydride transfer, and lactonization to provide novel lactone **P15** (Fig. 1d).

Through the efforts reported herein, 12 structurally complex compounds with novel ring systems were constructed from **P**, in addition to 6 compounds that had been previously reported; the majority of these were synthesized on ≥25 mg scale. In addition, the compound collection derived from **P** that was screened (vide infra) also included 11 compounds synthesized in our previously reported transformation of pleuromutilin to **P16** and carbocation rearrangement to afford bridged oxafenestranes such as **P17** (Fig. 1e).[33] The fraction of sp^3-hybridized carbons (Fsp3), the number of stereogenic centers, and ring complexity index were used as surrogates of complexity for the compounds synthesized from pleuromutilin, and these values compare favorably to compounds in screening collections as shown in the violin plots in Supplementary Figure 1.

Anticancer phenotypic screening and compound optimization

Compounds from **P** were evaluated in whole-cell assays for their ability to rapidly kill cancer cell lines in culture, starting with the ES-2 (ovarian cancer) cell line. All compounds were assessed at 12 μM, with cell viability determined using the Alamar Blue viability assay. Compounds that elicited at least 50% cell death were considered hit compounds and were then evaluated through full dose-response curves. From these assessments, compound **P4** was identified as having promising activity, with rapid induction of cell death (a phenotype discussed further below), an IC_{50} = 6.7 μM in ES-2 cells (Fig. 2a), and counter-screening revealed that this small molecule displayed no signs of hemolytic activity (Supplementary Fig. 1).

Modification of **P4** through a [4+2] cycloaddition provided compound **P18**, hereafter referred to as **ferroptocide** (Fig. 2a); this compound is more potent than **P4**, with an IC_{50} = 1.6 μM against ES-2 cells. Further modification of the secondary alcohol and the α-chloro ester of **ferroptocide** unveiled structural features important for activity. While methylation and acetylation of the secondary alcohol of **ferroptocide** (**P19** and **P20** respectively) did not

change the activity (Fig. 2b), replacement of the α-chloro ester with acetate (**P21**) eliminated activity. To investigate other electrophilic groups the fluoro-(**P22**) and iodo-(**P23**) compounds were synthesized. While **P22** had greatly diminished anticancer activity, iodo analogues (such as **P23**) showed greater potency in cells at the expense of biological selectivity (Supplementary Fig. 1), and because of this promiscuity such compounds were not pursued further. Additional compounds with poorer leaving groups such as α-acetate ester (**P24**), α,α dichloro ester (**P25**), and furoic ester (**P26**) exhibited no anticancer activity (Fig. 2b). Lead compound **ferroptocide** displays no antibacterial activity (MIC >64 μg/mL) in gram positive (*S. aureus*) or gram-negative (*E. coli*) bacteria but has robust anticancer activity in a panel of cancer cell lines and, notably, primary cancer cells freshly isolated from tumor tissues of 15 different patients with diverse metastatic cancers (Fig. 2c). **Ferroptocide** kills these cancer cells better than approved and experimental chemotherapeutics such as cisplatin, 5-FU, etoposide, and PAC-1 (Supplementary Fig. 1).

Additional synthesis and evaluation revealed that the N-N moiety in **ferroptocide** could be changed to C-C (**P28**, Fig. 2d), with minimal loss in activity. This discovery allowed for the construction of alkyne tool compound **P29** (Fig. 2d), which was subjected to a 1,3-dipolar cycloaddition resulting in fluorescent compound **P30**. Both **P29** and **P30** retained anticancer activity (Fig. 2d), and **P30** was used to report on subcellular localization. As shown by confocal microscopy, **P30** localizes to the cytoplasm in ES-2 cells (Fig. 2d), and this staining is competed away by pretreatment with **ferroptocide** (Supplementary Fig. 1). Importantly, installation of an α-chloro ester on pleuromutilin itself (**P27**), and other scaffolds such as lovastatin (**L1**), and quinine (**QQ1**), resulted in non-competing compounds in this localization experiment (Supplementary Fig. 1), demonstrating that the anticancer activity of **ferroptocide** is not attributed solely to the presence of the electrophilic functional group.

Ferroptocide induces non-apoptotic cell death

To gain insights into the mode of action, the speed of cell death of **ferroptocide** was compared to other approved chemotherapeutics and tool compounds with well-defined mechanisms including: procaspase-3 activators (PAC-1, 1541B),[34] nucleoside analogues (gemcitabine, 5-FU), DNA alkylators (MNNG, mitomycin C), topoisomerase inhibitors (etoposide, camptothecin, cycloheximide), reactive oxygen species (ROS) inducing agents (anitimycin A, IB-DNQ,[35] rotenone), broad-spectrum kinase inhibitor (staurosporine), microtubule stabilizer (taxol), proteasome inhibitor (bortezomib), and a rapid apoptosis-inducing agent (Raptinal).[36] The cell death induced by **ferroptocide** was rapid in multiple cell lines of diverse cancer types, with a time to 50% cell death of 1 hour in ES-2 (Fig. 3a), 1.5 hr in Mia PaCa-2 and 7 hr in HCT 116 cells (Supplementary Fig. 2). As the speed of cell death induced by **ferroptocide** was faster than the most rapid proapoptotic agent known (Raptinal), it was suspected to induce non-apoptotic cell death.

Time course analysis of cells treated with **ferroptocide** followed by Annexin V/PI staining indeed suggested a non-apoptotic mode of cell death (Fig. 3b), as did experiments showing that the pan-caspase inhibitor Q-VD-OPh does not protect against **ferroptocide**-induced cell death in ES-2 (Fig. 3c) and HCT 116 cells (Supplementary Fig 2). Cleavage of PARP-1 in **ferroptocide**-treated ES-2 or HCT 116 cells was not observed (Supplementary Fig. 2). As a

further confirmation, cell morphological changes induced by **ferroptocide** were examined using transmission electron microscopy (TEM). Cells treated with **ferroptocide** exhibit none of the apoptotic characteristics such as membrane blebbing and chromatin condensation (Fig. 3d, see staurosporine control). Together, these data indicate that **ferroptocide** induces rapid, non-apoptotic cell death. As compounds with such a mode of cell death can have unique properties and advantages in vivo,[37,38] further elucidation of the mechanism of cell death of **ferroptocide** was of interest.

Further analysis of the TEM images revealed mitochondrial swelling as early as 30 minutes after **ferroptocide** treatment. Subsequent confocal microscopy studies supported such findings as the fluorescent analogue **P30** was found to co-localize with the Mitotracker dye in cells (Fig. 3e) while the BODIPY azide dye alone did not (Supplementary Fig. 2), thus suggesting a mitochondria-based activity of **ferroptocide**. Given the importance of reactive oxygen species (ROS) generation in mitochondria, ROS levels were monitored upon compound treatment using a ROS probe, carboxy-H_2DCFDA. Dose-dependent ROS production was observed in ES-2 (Fig. 3f) and HCT 116 cells (Supplementary Fig. 2) treated with **ferroptocide**, similar to the positive control, *tert*-butyl hydroperoxide (TBHP). Furthermore, treatment of ES-2 cells with **ferroptocide** results in an increase of mitochondrial ROS similarly to treatment with positive controls IB-DNQ[39] and rotenone (Supplementary Fig. 2). Collectively, these data support a disruptive role of ferroptocide on mitochondrial activity.

Ferroptocide is a pro-ferroptotic agent

A non-apoptotic mode of cell death that depends on production of lethal levels of iron-dependent lipid ROS is ferroptosis, a regulated process with distinct morphological, biochemical, and genetic characteristics[40–44] that shares similar features with another non-apoptotic form of cell death, oxytosis[45–48]. The hallmarks of ferroptosis include generation of lipid hydroperoxides and cytoprotection by lipophilic antioxidants (trolox, butylated hydroxyltoluene [BHT]), ferroptosis inhibitors (ferrostatin-1, liproxstatin), and iron chelators (deferoxamine [DFO], ciclopirox olamine [CPX]).[40] Cellular effects of **ferroptocide**-induced ROS were investigated using a C11-BODIPY probe that responds to lipid peroxidation.[41] **Ferroptocide** induces lipid ROS in ES-2 (Fig. 4a), HCT 116, and 4T1 cells (Supplementary Fig. 3) similar to the known ferroptosis inducer, (1S,3R)-RSL3 (hereafter RSL3)[49] and/or TBHP; DFO pre-treatment of these cells abolishes each compound's activity. Given that generation of continuous lipid ROS is a functional requirement of ferroptosis,[40,41] additional experiments were conducted to elucidate if ferroptosis was triggered by **ferroptocide**. Protection studies were conducted with trolox, ferrostatin-1, and DFO, and all these inhibitors significantly protected against **ferroptocide**-induced cell death in ES-2 (Fig. 4 b, c, d), HCT 116, 4T1, and A549 cancer cells (Supplementary Fig. 3). Additionally, these inhibitors rescued cells from TBHP-treatment (Fig. 4b) and the known ferroptosis inducers erastin (Fig. 4c, d) and RSL3 (Supplementary Fig. 3) respectively, while they showed no protection against Raptinal, an apoptosis-inducing agent. Treatment of HCT 116 and A549 cells with the antioxidant N-acteyl cysteine (NAC-1) resulted in protection from **ferroptocide**- and TBHP-induced cell death but not Raptinal (Supplementary Fig. 3). Together, these studies indicate that iron-dependent

accumulation of lipid peroxidation (ferroptosis) upon **ferroptocide**-treatment is the cause of cell death.

Erastin and RSL3 were originally discovered as small molecules with RAS-selective lethality.[41] Monitoring of speed of cell death of **ferroptocide** versus erastin and RSL3 in HCT 116 and A549 cells (which contain mutant oncogenic K-RAS), demonstrates that **ferroptocide** is a fast-acting, robust pro-ferroptotic agent inducing more quantitative cell death than the other tool compounds (Fig. 4e). Additionally, treatment of HCT 116 cells with the same concentration of these compounds results in generation of similar levels of lipid ROS upon **ferroptocide** and RSL3 treatment and a larger quantity compared to erastin-treatment, suggesting a rapid onset of lipid peroxidation for **ferroptocide** and RSL3 (Supplementary Fig. 3). Given that RSL3 is a covalent inhibitor of a central regulator of ferroptosis, GPX4,[40,45] we monitored if **ferroptocide** modulates the activity of GPX4 in cells. As shown in Supplementary Fig. 3, treatment of ES-2 cells with **ferroptocide** did not result in GPX4 inhibition (in contrast to the positive control RSL3), suggesting a different target for **ferroptocide**.

Further experiments were conducted to monitor the effect of **ferroptocide** at the transcript level. RNA-seq data of **ferroptocide**-treated cells revealed that 35/40 genes involved in ferroptosis are modulated with false discovery rate (FDR) scores ≤0.05 upon 6 hr treatment (Supplementary Fig. 3). This time point was selected to capture the primary mechanisms of the compound of interest on viable cells (Supplementary Fig. 3) as described previously.[50] Specific genes such as GCLC (3.5 fold), GCLM (4.9 fold), SLC7A11 (8.1 fold), CHAC1 (9.8 fold) known to be upregulated in ferroptosis[40,51] and endoplasmic reticulum stress (ATF3 11.5 fold, DDIT3 22.5 fold, DDIT4 11.3 fold), were significantly upregulated after **ferroptocide**-treatment, similar to RNA-seq reports for erastin in HT-1080 cells.[51] Pathways affected by oxidative stress such as Keap1-Nrf2 ($p=7.8\ 10^{-10}$), unfolded protein response ($p=3.6\ 10^{-8}$), protein processing in endoplasmic reticulum ($p=2.4\ 10^{-10}$), and others were also modified upon compound treatment (Supplementary Fig. 3 and Data Package 1). These transcription profiles provide further support that **ferroptocide** induces oxidative stress and ferroptosis.

Ferroptocide covalently modifies thioredoxin

SAR trends reveal that **ferroptocide-**bioactivity depends on the presence of the electrophilic α-chloroester (Fig. 2), suggesting covalent modification of its target. In vitro studies indicate that **ferroptocide** reacts slowly with excess glutathione (67% compound remaining after 2 hr) compared to the rapid reaction of the promiscuous iodo analogue, **P23** (Supplementary Fig. 4). To assess covalent modification in cells, in-gel fluorescence studies were performed in conjunction with competition studies. Treatment of HCT 116 cells with increasing concentrations of fluorescent analogue **P30** resulted in labeling of five main bands (Fig. 5a). Pretreatment of cells with various concentrations of **ferroptocide**, followed by treatment with **P30** resulted in dose-dependent competition, primarily of two bands, in the in-gel fluorescence assay (bands B and D in Fig. 5b). A similar labeling and competition pattern was observed in multiple cancer cell lines, including HCT 116, ES-2, U937, MIA PaCa-2,

BT-549, T47D, MDA-MB-231 (Fig. 5c), and primary cancer cells from patients (Fig. 5d), suggesting modulation of the same targets in immortalized and in primary cancer cells.

In an effort to identify the labeled protein(s), a biotin-streptavidin pulldown[52] (Schematic in Fig. 5e) was performed with alkyne **P29**. Briefly, HCT 116 cells were pre-treated with **ferroptocide** or DMSO, followed by treatment with **P29**. Upon incorporation of a biotin, **P29**-labeled proteins were enriched on streptavidin beads, subjected to an on-bead trypsin digestion and subsequent LC/LC–MS/MS analysis. Protein identities were determined by database searches using the SEQUEST algorithm. Relative quantitation of proteins enriched in **ferroptocide** and DMSO pre-treated samples was achieved by spectral counting (Fig. 5f). High-affinity targets from the HCT 116 cell line were then compared to targets identified in ES-2 cells (Data Package 2). Based on shared enrichment in both cell lines, as well as molecular weights matching the gel bands, nine proteins were selected for follow up characterization (Fig. 5g). Importantly, GPX4 protein was not identified as a target of interest for **ferroptocide**, with low spectral counts below the cutoff for significance.

In order to discriminate between on- and off-cytotoxicity-related targets, siRNA and CRISPR Cas9 strategies were employed. Upon successful siRNA knockdown of KEAP1 and GSTO1, an assessment was made of how changes in protein expression affected band labeling in gels. Comparison of cells with knockdown targets and wild type cells indicated no change in in-gel fluorescence (Supplementary Fig 5), suggesting that KEAP1 and GSTO1 are off-pathway targets of **ferroptocide**. CRISPR Cas9 technology was then used to rapidly investigate the remaining targets. We were able to successfully generate isogenic cell line pairs for six knockout targets, with one other target being lethal. Knockout of six targets did not diminish labeling of any of the fluorescent bands indicating that such proteins (PTGES2, PGLS, TXNRD1, TXNRD2, TXNRD3, and PDP1) were not the targets of interest (Supplementary Fig. 5), while the lethal target corresponded to that of thioredoxin protein.

Thioredoxin (TXN) is a 12 kDa ubiquitous oxidoreductase that plays a key role in the thioredoxin antioxidant system comprised of thioredoxin, NADPH, and thioredoxin reductase. Thioredoxin contains five cysteines and uses active site cysteines (C32 and C35) to reduce the disulfide bonds of many protein partners such as transcription factors (NF-κB, AP-1, Ref-1), ribonucleotide reductases, peroxiredoxins, and glutathione peroxidases, as well as scavenging of ROS.[53,54] Treatment of HCT 116 cells with **P29**, coupled to biotin-streptavidin enrichment followed by immunoblotting yielded a band present only in compound treated sample (Fig. 6a), suggesting that **ferroptocide** covalently modifies thioredoxin. A thioredoxin activity assay was then employed to assess the ability of **ferroptocide** to inhibit thioredoxin activity in cell lysate. **Ferroptocide** significantly reduced the activity of thioredoxin (Trx) in ES-2 cells to a greater extent than the two known inhibitors of thioredoxin (PMX464 and PX-12)[55–57] (Fig. 6b). Dose-response analysis confirmed that **ferroptocide** is also a more potent thioredoxin inhibitor than PMX464 and PX-12 in a biochemical (*in vitro*) assay (Supplementary Fig. 5).

To further assess the effect of **ferroptocide** on thioredoxin, thioredoxin fused to GFP (TXN-GFP, 37kDa) was overexpressed in HCT 116 cells (Supplementary Fig. 5). Treatment of

these cells with **P29**, followed by bioconjugation of the orthogonal fluorophore of Cy3, afforded the expected band at 37 kDa (Fig. 6c), which was competed by **ferroptocide**. To identify the sites of modification of thioredoxin by **ferroptocide**, site-directed mutagenesis introduced serine mutants of each of the five cysteines of TXN-GFP. The ability of **ferroptocide** to covalently modify these mutant proteins (C32S, C35S, C62S, C69S, and C73S, Supplementary Fig. 5) was assessed in a fluorescent band labeling experiment. As shown in Figure 6d, the 37 kDa band is not present in the C32S and C35S mutants and has reduced labeling in the C73S mutant, suggesting that **ferroptocide** is modifying the active site cysteines and the adjacent cysteine 73 of thioredoxin as shown in the crystal structure (Fig. 6e). Taken together, these studies demonstrate that treatment with **ferroptocide** modifies critical residues needed for interaction of thioredoxin with its binding partners, and thus inhibiting its activity in cells. This inhibition presumably causes the observed phenotype of rapid ferroptotic cell death. Given that thioredoxin is a key component of a major antioxidant system, it is possible that its modulation renders cells susceptible to oxidative stress that causes lipid peroxidation and other imbalances in cellular processes which eventually lead to ferroptotic cell death; other thioredoxin inhibitors have not been reported to induce ferroptosis.

General and lipid ROS levels were monitored upon genetic knockdown of thioredoxin in HCT 116 cells. Knockdown of thioredoxin (siTXN) resulted in massive generation of general ROS and lipid ROS within 72 hr (Supplementary Fig. 6) consistent with induction of ferroptosis. Pretreatment of HCT 116 cells with ferroptosis inhibitors of trolox and ferrostatin-1 did not protect against siTXN, however, likely due to high ROS levels and long incubation times required for sufficient knockdown of thioredoxin; pretreatment with DFO impaired cell viability even in the control HCT 116 cells transfected with scrambled RNA (siNeg, Supplementary Fig. 6). In order to determine if thioredoxin inhibitors cause ferroptotic cell death, protection studies with ferroptosis inhibitors were conducted in two cell lines; minimal protection was observed in ES-2 cells while A549 displayed no change in cell death compared to untreated cells (Supplementary Fig. 6). These results are unsurprising given that PMX464[55,58] and PX-12[59,60] are imperfect tool compounds, suspected to engage multiple molecular targets in cells. The siRNA knockdown of thioredoxin sensitizes HCT116 cells to **ferroptocide** but not Raptinal treatment in a time course study (Fig. 6f and Supplementary Fig. 6), further suggestive of the importance of thioredoxin in **ferroptocide**-induced cell death. Together, these data support a role of thioredoxin in **ferroptocide**-induced cell death and ferroptosis.

Ferroptocide is an immunostimulatory compound

The non-apoptotic nature of **ferroptocide** inspired preliminary exploration of its ability to modulate the immune system. Non-apoptotic compounds are attractive anticancer agents, as they can potentially elicit an immune response.[37] Ferroptocide displays some activity in non-cancerous breast (MCF10A) and human skin fibroblast (HFF-1) cells (IC_{50} of 3.1 and 4.1 μM respectively) but no hemolytic activity, so it is a favorable tool compound to assess *in vivo*. We investigated the role of the immune system by assessing the efficacy of **ferroptocide** in a subcutaneous murine model of 4T1 triple negative breast cancer cells in immunocompetent (Balb/c) compared to immunocompromised (SCID) mice. Measurements

of tumor volume indicated a 40% tumor growth retardation in compound-treated Balb/c compared to vehicle-treated mice, with activity likely limited by poor compound pharmacokinetics in mice (Fig 7 and Supplementary Fig. 7). The lack of activity in immunocompromised mice suggests that T and B cells play a role in the activity of **ferroptocide** in vivo.

Conclusions

Small molecules are powerful tools to investigate protein function and cell death mechanisms. Staurosporine and more recently Raptinal[36] are commonly used to predictably and rapidly induce apoptotic cell death, and enable the study of its mechanisms and protein regulators. Selective inhibitors of cell death processes are also extremely valuable, with z-VAD-fmk and Q-VD-OPh widely used to inhibit apoptosis, and necrostatin-1 and ferrostatin-1 used to inhibit necrosis and ferroptosis, respectively.[61]

In contrast to the variety of tool compounds available to induce apoptosis, there are comparatively fewer that can be used to induce ferroptosis, another regulated form of cell death.[62] Erastin and RSL3 are the first reported inducers of ferroptosis, followed by more recent reports of salinomycin,[63] sorafenib, FIN56, and $FINO_2$.[40] These compounds have been instrumental in the discovery of ferroptosis and elucidation of key ferroptotic regulators (system x_c^- and glutathione peroxidase 4) and related pathways. However, these compounds typically do not induce quantitative cell death, and lack potent lethality in multiple cell lines, revealing a need for additional pro-ferroptotic agents. Furthermore, the discovery of other inducers of ferroptosis can uncover additional proteins critical to this cell death process.

Herein, we report the application of the CtD strategy to the natural product of pleuromutilin that provided a set of 29 structurally diverse and highly complex compounds. This set was then subjected to a phenotypic screen that allowed discovery of **ferroptocide**, which induces rapid ferroptotic death in immortalized cancer cell lines and primary cancer cells from patients. Cell culture studies demonstrate that **ferroptocide**-treated cells generate ROS and lipid peroxidation that result in inevitable cell death, an effect that can be prevented by pretreatment with known inhibitors of ferroptosis (trolox, ferrostatin-1, and DFO). Depletion of the glutathione antioxidant system and pharmacological inhibition or degradation of glutathione peroxidase 4 (GPX4) are the main known systems that control ferroptosis.[40,41,43,44,51,64] In contrast, the collected data suggest that **ferroptocide** targets a different antioxidant system (thioredoxin) to induce ferroptosis; it is likely that inhibition of thioredoxin causes a drastic imbalance in the ROS levels, overwhelms cellular antioxidant responses (as seen at the transcript level), and causes ferroptosis. This hypothesis is supported by genetic knockdown studies of thioredoxin, which lead to accumulation of large amounts of ROS, lipid ROS and sensitization of siTXN cells to **ferroptocide** treatment. Nevertheless, further mechanistic details of the thioredoxin-ferroptosis link remain to be understood, and the possibility that there are alternative targets important for the pro-ferroptotic action of **ferroptocide** cannot be ruled out.

Head-to-head comparisons of **ferroptocide** to erastin and RSL3 suggest that **ferroptocide** may have advantages, especially for applications requiring induction of rapid and/or quantitative ferroptotic cell death. Furthermore, as **ferroptocide** induces a regulated, non-apoptotic mode of cell death, this compound (and possibly other pro-ferroptotic agents) have the potential to synergize with the immune system for the treatment of cancer. **Ferroptocide** represents a distinct class of ferroptosis inducers and will be an important tool compound for further studies of ferroptosis.

Methods

Full experimental details and characterization data for all new compounds are included in the Supplementary Information.

Data Availability

The data supporting the findings of this study are available within the paper and supplementary information and are available from the corresponding author upon request. The mass spectrometry proteomics data have been deposited to the ProteomeXchange Consortium via the PRIDE partner repository with the dataset identifier PXD012805. The RNA sequencing data have been deposited to the GEO repository with the accession number GSE126868. The X-ray crystallography data have been deposited in the Cambridge Crystallographic Data Center (CCDC) using the following identifiers: 1851845 (compound P1) and 1849494 (Ferroptocide).

Supplementary Material

Refer to Web version on PubMed Central for supplementary material.

Acknowledgements

We are grateful to the University of Illinois and Cancer Scholars for Translational and Applied Research (C*STAR) program for support of this work, and for the NIH (R01GM118575) for support of some of the synthetic studies. We would like to thank Wendy Woods and Dr. Pablo Perez Pinera for their assistance with CRISPR Cas9 studies, Dr. Danielle Gray and Dr. Toby Woods for X-ray analysis of compounds, Professor Levent Dirikolu for calculation of PK parameters, Bryon Drown for chemoinformatic analysis of compounds, Michael E. Vinyard and Adam Sowers for synthetic assistance, and Dr. Sarah Tasker for many helpful discussions.

References

1. Lovering F, Bikker J & Humblet C Escape from flatland: Increasing saturation as an approach to improving clinical success. J. Med. Chem 52, 6752–6756, (2009). [PubMed: 19827778]
2. Swinney DC & Anthony J How were new medicines discovered? Nat. Rev. Drug Discov 10, 507–519, (2011). [PubMed: 21701501]
3. Galloway WRJD, Isidro-Llobet A & Spring DR Diversity-oriented synthesis as a tool for the discovery of novel biologically active small molecules. Nat. Commun 1, 80–93, (2010). [PubMed: 20865796]
4. Gerry CJ & Schreiber SL Chemical probes and drug leads from advances in synthetic planning and methodology. Nat. Rev. Drug Discov 17, 333–352, (2018). [PubMed: 29651105]
5. Morrison KC & Hergenrother PJ Natural products as starting points for the synthesis of complex and diverse compounds. Nat. Prod. Rep 31, 6–14, (2014). [PubMed: 24219884]

6. Huigens RW III et al. A ring-distortion strategy to construct stereochemically complex and structurally diverse compounds from natural products. Nat. Chem 5, 195–202, (2013). [PubMed: 23422561]
7. Ciardiello JJ et al. A novel complexity-to-diversity strategy for the diversity-oriented synthesis of structurally diverse and complex macrocycles from quinine. Bioorg. Med. Chem 25, 2825–2843, (2017). [PubMed: 28283333]
8. Rafferty RJ, Hicklin RW, Maloof KA & Hergenrother PJ Synthesis of complex and diverse compounds through ring distortion of abietic acid. Angew. Chem. Int. Ed 53, 220–224, (2014).
9. Garcia A, Drown BS & Hergenrother PJ Access to a structurally complex compound collection via ring distortion of the alkaloid sinomenine. Org. Lett 18, 4852–4855, (2016). [PubMed: 27650404]
10. Tasker SZ, Cowfer AE & Hergenrother PJ Preparation of Structurally Diverse Compounds from the Natural Product Lycorine. Org. Lett 20, 5894–5898, (2018). [PubMed: 30204451]
11. Paciaroni NG et al. A tryptoline ring-distortion strategy leads to complex and diverse biologically active molecules from the indole alkaloid yohimbine. Chem. Eur. J 23, 4327–4335, (2017). [PubMed: 27900785]
12. Govindaraju K et al. Novel topologically complex scaffold derived from alkaloid haemanthamine. Molecules 23, 255–263, (2018).
13. Charaschanya M & Aubé J Reagent-controlled regiodivergent ring expansions of steroids. Nat. Commun 9, 934–942, (2018). [PubMed: 29507290]
14. Laurent E et al. A ring-distortion strategy from marine natural product ilimaquinone leads to quorum sensing modulators. Eur. J. Org. Chem 2018, 2486–2497, (2018).
15. Xu H et al. Identification of a diverse synthetic abietane diterpenoid library for anticancer activity. Bioorg. Med. Chem. Lett 27, 505–510, (2017). [PubMed: 28011223]
16. Luca L et al. Discovery of novel cinchona-alkaloid-inspired oxazatwistane autophagy inhibitors. Angew. Chem. Int. Ed 56, 2145–2150, (2017).
17. Richter MF et al. Predictive compound accumulation rules yield a broad-spectrum antibiotic. Nature 545, 299–304, (2017). [PubMed: 28489819]
18. Poulsen SM, Karlsson M, Johansson LB & Vester B The pleuromutilin drugs tiamulin and valnemulin bind to the RNA at the peptidyl transferase centre on the ribosome. Molecular Microbiology 41, 1091–1099, (2001). [PubMed: 11555289]
19. Ma X et al. Directed C–H bond oxidation of (+)-pleuromutilin. J. Org. Chem 83, 6843–6892, (2018). [PubMed: 29664634]
20. Farney EP, Feng SS, Schäfers F & Reisman SE Total synthesis of (+)-pleuromutilin. J. Am. Chem. Soc 140, 1267–1270, (2018). [PubMed: 29323492]
21. Murphy SK, Zeng M & Herzon SB A modular and enantioselective synthesis of the pleuromutilin antibiotics. Science 356, 956–959, (2017). [PubMed: 28572392]
22. Thirring K, et al. & 12-epi-pleuromutilins. U.S. WO2015110481A1 patent (2015).
23. Gibbons EG Total synthesis of (.+−.)-pleuromutilin. J. Am. Chem. Soc 104, 1767–1769, (1982).
24. Paquette LA, Wiedeman PE & Bulman-Page PC (+)-Pleuromutilin synthetic studies. Degradative and de novo acquisition of a levorotatory tricyclic lactone subunit. J. Org. Chem 53, 1441–1450, (1988).
25. Liu J, Lotesta SD & Sorensen EJ A concise synthesis of the molecular framework of pleuromutilin. Chem. Commun 47, 1500–1502, (2011).
26. Birch AJ, Holzapfel CW & Rickards RW The structure and some aspects of the biosynthesis of pleuromutilin. Tetrahedron 22, 359–387, (1966).
27. Arigoni D Some studies in the biosynthesis of terpenes and related compounds. Pure Appl. Chem 17, 331–348, (1968). [PubMed: 5729285]
28. Drews J et al. Antimicrobial activities of 81.723 hfu, a new pleuromutilin derivative. Antimicrob. Agents Chemother 7, 507–516, (1975). [PubMed: 1170807]
29. Yang LHK, Retapamulin S: a review of its use in the management of impetigo and other uncomplicated superficial skin infections. Drugs 68, 855–873, (2008). [PubMed: 18416589]

30. Berner H, Schulz G & Schneider H Synthese ab-trans-anellierter derivate des tricyclischen diterpens pleuromutilin durch intramolekulare 1,5-hydrid-verschiebung. Tetrahedron 36, 1807–1811, (1980).
31. Andemichael Y et al. Process development for a novel pleuromutilin-derived antibiotic. Org. Process Res. Dev 13, 729–738, (2009).
32. Uccello DP et al. The synthesis of C-13 functionalized pleuromutilins via C–H amidation and subsequent novel rearrangement product. Tetrahedron Lett 52, 4247–4251, (2011).
33. Hicklin RW, López Silva T. L. & Hergenrother PJ Synthesis of bridged oxafenestranes from pleuromutilin. Angew. Chem. Int. Ed 53, 9880–9883, (2014).
34. Botham RC et al. Dual small-molecule targeting of procaspase-3 dramatically enhances zymogen activation and anticancer activity. J. Am. Chem. Soc 136, 1312–1319, (2014). [PubMed: 24383395]
35. Parkinson EI, Bair JS, Cismesia M & Hergenrother PJ Efficient NQO1 substrates are potent and selective anticancer agents. ACS Chem. Biol 8, 2173–2183, (2013). [PubMed: 23937670]
36. Palchaudhuri R et al. A small molecule that induces intrinsic pathway apoptosis with unparalleled speed. Cell Rep 13, 2027–2036.
37. Linkermann A, Stockwell BR, Krautwald S & Anders H-J Regulated cell death and inflammation: an auto-amplification loop causes organ failure. Nat. Rev. Immunol 14, 759–767, (2014). [PubMed: 25324125]
38. Galluzzi L, Senovilla L, Zitvogel L & Kroemer G The secret ally: Immunostimulation by anticancer drugs. Nat. Rev. Drug Discov 11, 215–233, (2012). [PubMed: 22301798]
39. Lee HY et al. Reactive Oxygen Species Synergize To Potently and Selectively Induce Cancer Cell Death. ACS Chem. Biol 12, 1416–1424, (2017). [PubMed: 28345875]
40. Stockwell BR et al. Ferroptosis: A regulated cell death nexus linking metabolism, redox biology, and disease. Cell 171, 273–285, (2017). [PubMed: 28985560]
41. Dixon Scott J. et al. Ferroptosis: An iron-dependent form of nonapoptotic cell death. Cell 149, 1060–1072.
42. Yang WS et al. Regulation of ferroptotic cancer cell death by GPX4. Cell 156, 317–331, (2014). [PubMed: 24439385]
43. Shimada K et al. Global survey of cell death mechanisms reveals metabolic regulation of ferroptosis. Nat. Chem. Biol 12, 497–503, (2016). [PubMed: 27159577]
44. Gaschler MM et al. FINO2 initiates ferroptosis through GPX4 inactivation and iron oxidation. Nat. Chem. Biol 14, 507–515, (2018). [PubMed: 29610484]
45. Lewerenz J et al. Oxytosis/Ferroptosis—(Re-) Emerging Roles for Oxidative Stress-Dependent Non-apoptotic Cell Death in Diseases of the Central Nervous System. Front. Neurosci 12, 214, (2018). [PubMed: 29731704]
46. Murphy TH et al. Calcium-dependent glutamate cytotoxicity in a neuronal cell line. Brain Res 444, 325–332, (1988). [PubMed: 2896063]
47. Miyamoto M, Murphy TH, Schnaar RL & Coyle JT Antioxidants protect against glutamate-induced cytotoxicity in a neuronal cell line. J. Pharmacol. Exp. Ther 250, 1132–1140, (1989). [PubMed: 2778712]
48. Seiler A et al. Glutathione Peroxidase 4 Senses and Translates Oxidative Stress into 12/15-Lipoxygenase Dependent- and AIF-Mediated Cell Death. Cell Metabolism 8, 237–248, (2008). [PubMed: 18762024]
49. Yang WS & Stockwell BR Synthetic lethal screening identifies compounds activating iron-dependent, nonapoptotic cell death in oncogenic-RAS-harboring cancer cells. Chem. Biol 15, 234–245, (2008). [PubMed: 18355723]
50. Subramanian A et al. A next generation connectivity map: L1000 platform and the first 1,000,000 profiles. Cell 171, 1437–1452.
51. Dixon SJ et al. Pharmacological inhibition of cystine–glutamate exchange induces endoplasmic reticulum stress and ferroptosis. eLife 3, e02523, (2014). [PubMed: 24844246]

52. Banerjee R, Pace NJ, Brown DR & Weerapana E 1,3,5-Triazine as a modular scaffold for covalent inhibitors with streamlined target identification. J. Am. Chem. Soc 135, 2497–2500, (2013). [PubMed: 23379904]

53. Holmgren A Thioredoxin structure and mechanism: conformational changes on oxidation of the active-site sulfhydryls to a disulfide. Structure 3, 239–243, (1995). [PubMed: 7788289]

54. Nordberg J & Arnér ESJ Reactive oxygen species, antioxidants, and the mammalian thioredoxin system. Free Radical Biol. Med 31, 1287–1312, (2001). [PubMed: 11728801]

55. Mukherjee A et al. A cellular and molecular investigation of the action of PMX464, a putative thioredoxin inhibitor, in normal and colorectal cancer cell lines. Br. J. Pharmacol 151, 1167–1175, (2007). [PubMed: 17572693]

56. Baker AF et al. The antitumor thioredoxin-1 inhibitor PX-12 (1-methylpropyl 2-imidazolyl disulfide) decreases thioredoxin-1 and VEGF levels in cancer patient plasma. J. Lab. Clin. Med 147, 83–90, (2006). [PubMed: 16459166]

57. Kirkpatrick DL et al. Mechanisms of inhibition of the thioredoxin growth factor system by antitumor 2-imidazolyl disulfides. Biochem. Pharmacol 55, 987–994, (1998). [PubMed: 9605422]

58. Sexton DW Targeting airway inflammation: PMX464 and the epithelial bulls eye. Br. J. Pharmacol 155, 620–622, (2008). [PubMed: 18604227]

59. Reynoso E et al. Thioredoxin-1 actively maintains the pseudokinase MLKL in a reduced state to suppress disulfide bond-dependent MLKL polymer formation and necroptosis. J. Biol. Chem, 17514–17524, (2017). [PubMed: 28878015]

60. You BRS,HR; Park WH PX-12 inhibits the growth of A549 lung cancer cells via G2/M phase arrest and ROS-dependent apoptosis. Int. J. Oncol 44, 301–308, (2014). [PubMed: 24172913]

61. Li Y, Qian L & Yuan J Small molecule probes for cellular death machines. Curr. Opin. Chem. Biol 39, 74–82, (2017). [PubMed: 28628894]

62. Galluzzi L et al. Molecular mechanisms of cell death: Recommendations of the Nomenclature Committee on Cell Death 2018. Cell Death Differ 25, 486–541, (2018). [PubMed: 29362479]

63. Mai TT et al. Salinomycin kills cancer stem cells by sequestering iron in lysosomes. Nat. Chem 9, 1025–1033, (2017). [PubMed: 28937680]

64. Bruni A et al. Ferroptosis-inducing agents compromise in vitro human islet viability and function. Cell Death Dis 9, 595–605, (2018). [PubMed: 29789532]

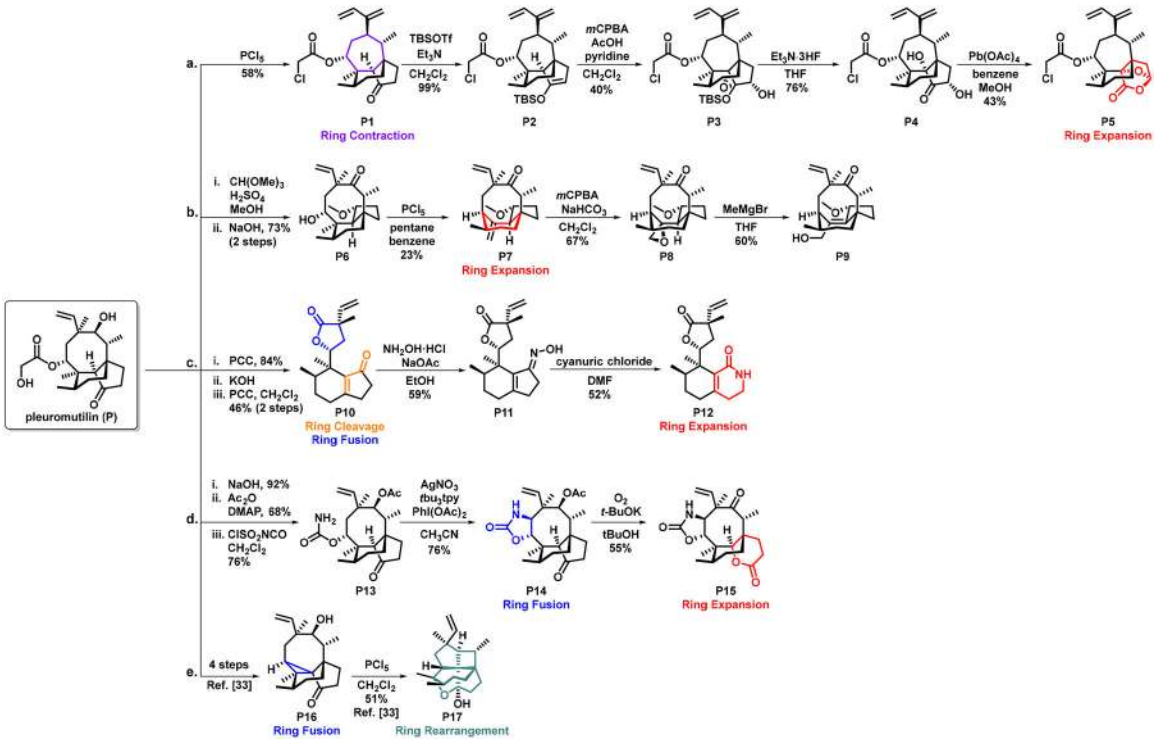

Figure 1: Compounds synthesized via ring system distortion of pleuromutilin using the CtD strategy.

a. Synthetic route to **P5** from **P** using a ring contraction of the 8-membered ring followed by a Rubottom oxidation and oxidative cleavage. **b**. Synthetic route to **P9** from **P** using ring expansion, diastereoselective epoxidation and elimination. **c**. Synthetic route to lactam **P12** from **P** using a retro-Michael ring cleavage and oxidative rearrangement followed by a Beckmann ring expansion. **d**. Synthetic route to **P15** upon ring fusion of **P** by C–H amidation followed by alkaline autoxidation, hydride migration, and lactonization. **e**. Synthesis of oxafenestranes from **P** as described previously.[33]

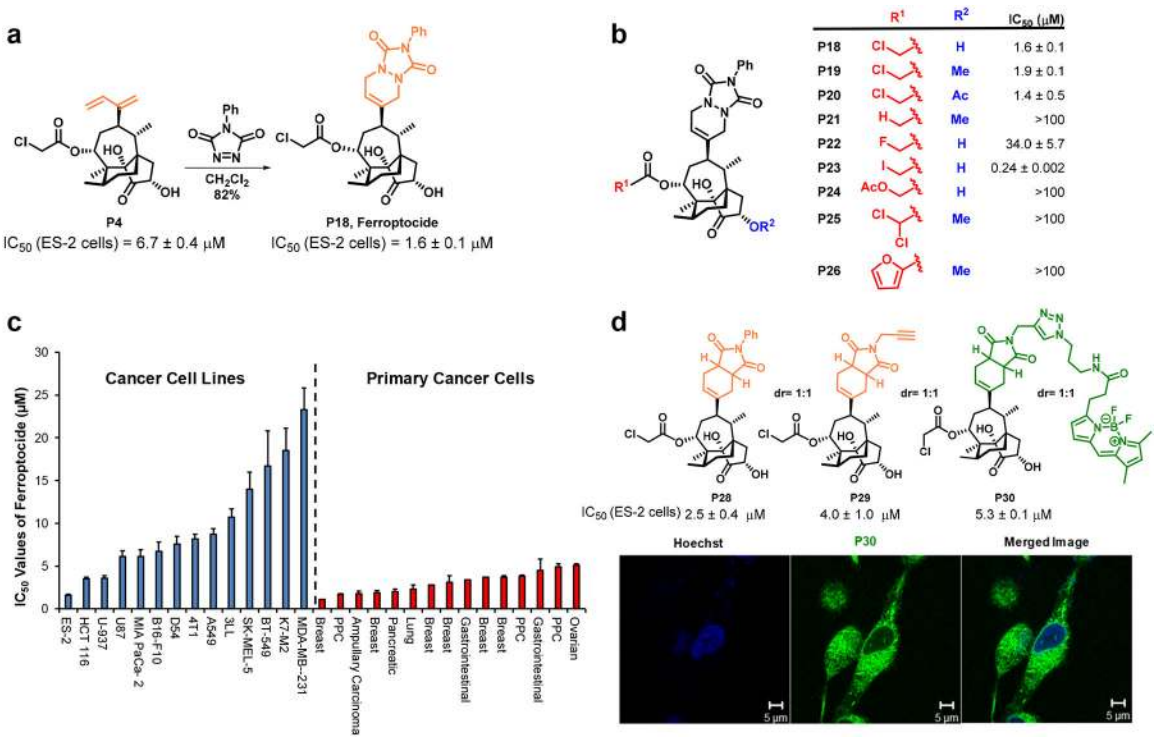

Figure 2: Synthesis and evaluation of ferroptocide.

a. Structure of P4, a hit compound in the cytotoxic phenotypic screen. Synthesis of lead compound **P18** (hereafter, **ferroptocide**). Below each compound is their respective 72 hr half-maximal inhibitory concentration (IC_{50}) value against ES-2 cells. Data represent the mean ± s.e.m., n=3 biological replicates. **b**. Structure–activity relationship studies of **P18** analogues, bioactivity is expressed as a 72 hr IC_{50} value against ES-2 cell line as measured by Alamar Blue fluorescence. Data represent the mean ± s.e.m., n=3 biological replicates. **c**. Ferroptocide displays broad activity in a 72 hr cell viability assay in immortalized cancer cells and in primary cells isolated from metastatic cancer patients. PPC: primary peritoneal carcinoma. Data represent the mean ± s.e.m., n=3 biological replicates. **d**. Tool compounds **P28**, **P29**, and **P30** retain biological activity in a 72 hr cell viability assay in ES-2 cells. Confocal microscopy images of ES-2 cells treated with fluorescent analogue, **P30** (1 μM) for 15 min show non-nuclear localization (green). Nucleus was stained with Hoechst (blue) n=3 biological replicates.

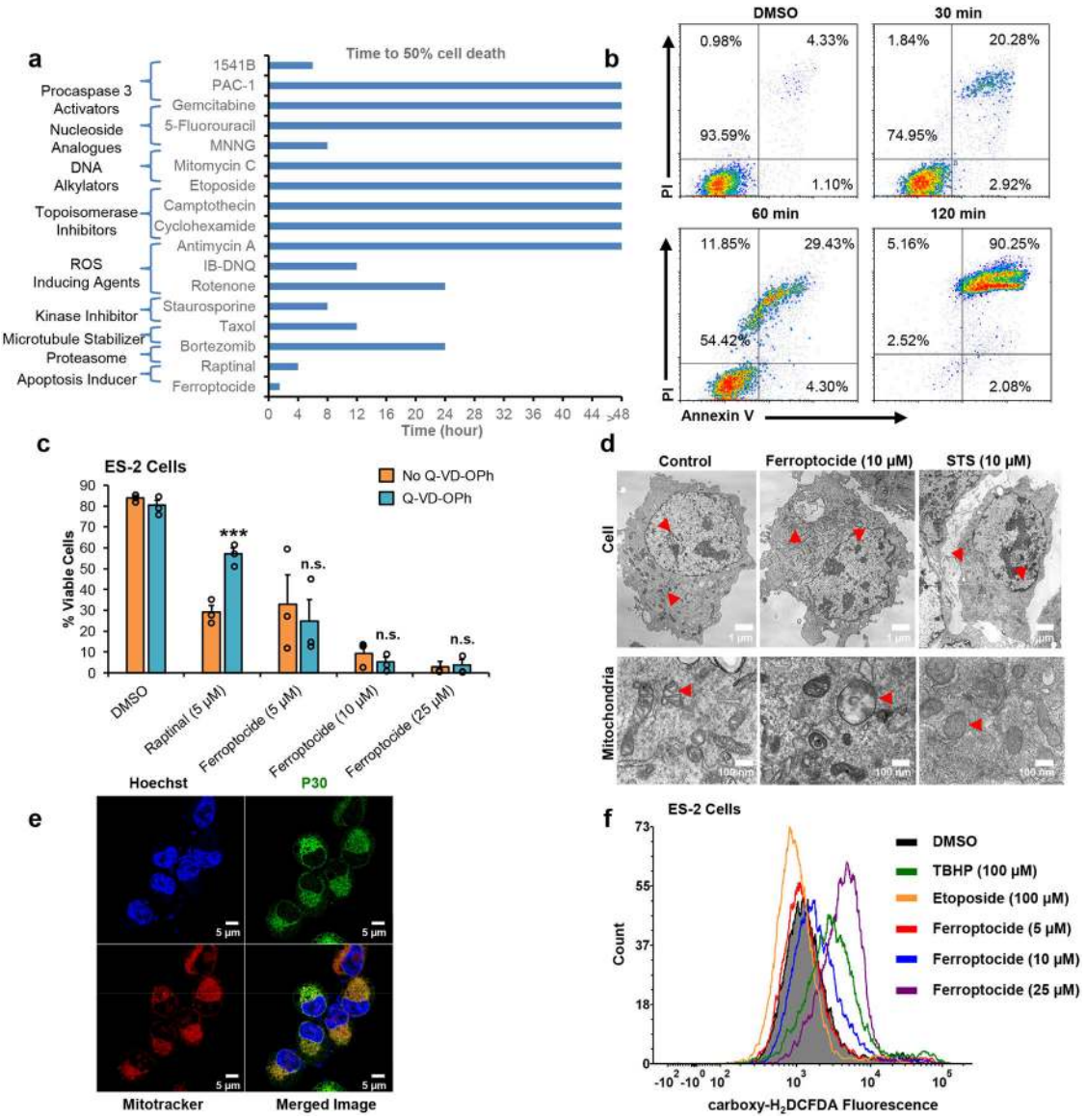

Figure 3: Ferroptocide induces rapid non-apoptotic cell death.

a. Speed of death of cells treated with ferroptocide versus 16 other anticancer compounds in ES-2 cells (all tested at 10 μM). Cell viability was assessed by AV/PI analysis. Representative data shown from full time course data (three biological replicates) in Supplementary Fig. 8. **b**. Time-course analysis of ES-2 cell viability upon treatment with ferroptocide (10 μM) indicates a non-apoptotic mode of cell death. AV/PI graphs are representative of three biological replicates. **c**. Effect of pretreatment with Q-VD-OPh (25 μM) for 2 hr followed by dose-response treatment with ferroptocide or positive control Raptinal (5 μM) for 13 hr in ES-2 cells. Data are plotted as the mean ± s.e.m., n=3 biological replicates. Two-sided t-test, ***P = 0.0003, n.s. P > 0.05. **d**. Transmission electron micrographs of ES-2 cells treated with DMSO (left), ferroptocide (10 μM, center) or staurosporine (STS, 10 μM, right) for 30 min. The images show lack of apoptotic morphological features and swelling of mitochondria upon ferroptocide treatment (red

arrows) versus controls. TEM data are representative images of three technical replicates. **e**. Co-localization analysis with mitochondria. ES-2 cells were stained with MitoTracker Red (100 nM) followed by 30 min treatment with fluorescent analogue **P30** (10 μM). Nucleus was stained with Hoechst. Yellow dots indicate **P30** (green) on the mitochondria (red) in merged images, n=3 independent experiments. **f**. Ferroptocide induces dose-dependent ROS generation within 1 hr similar to positive control TBHP in ES-2 cells (and also in HCT 116 cells, see Supplementary Fig. 2). DMSO and etoposide were included as negative controls. Data are representative of three independent experiments.

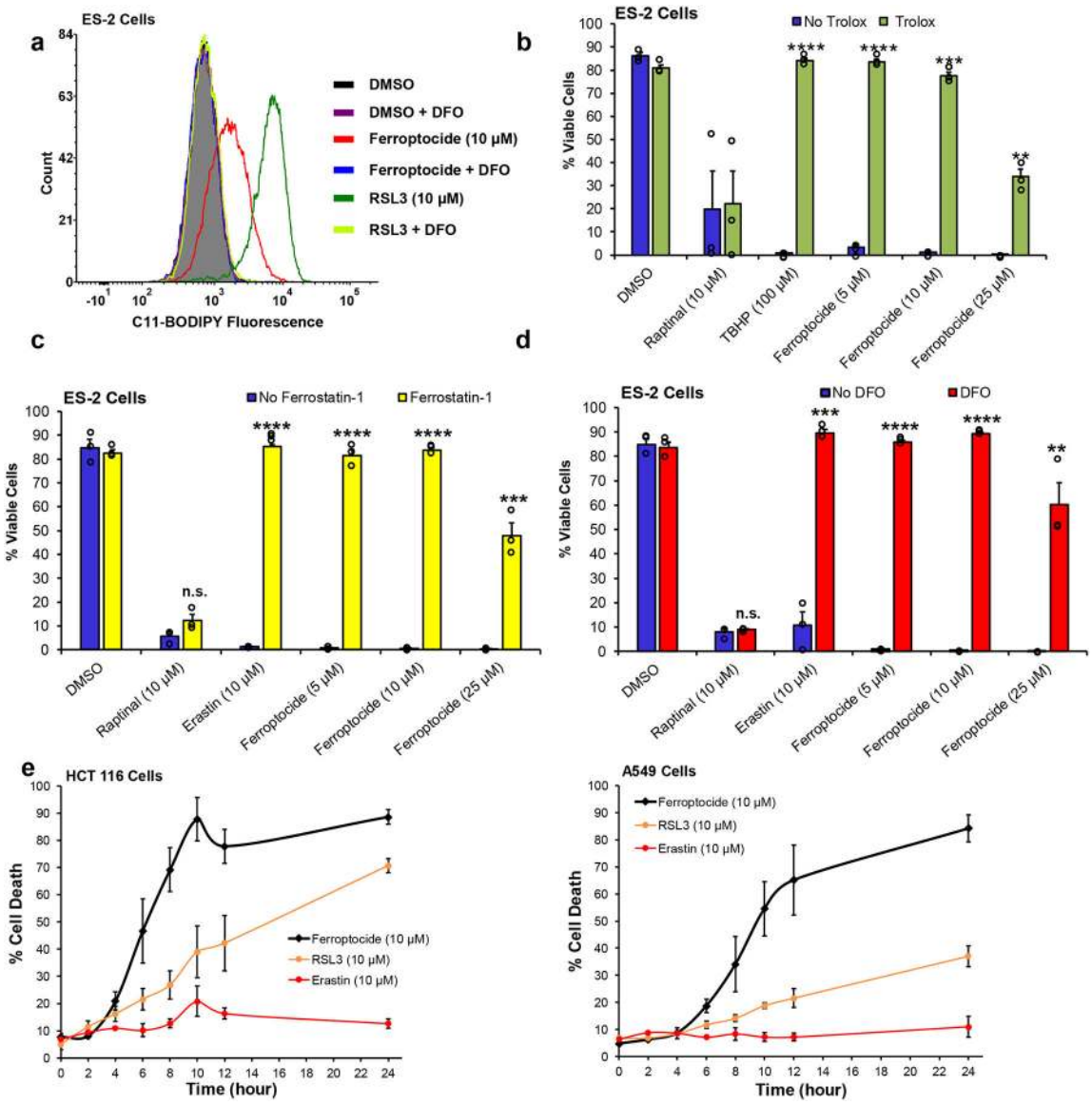

Figure 4: Ferroptocide kills cancer cells through ferroptosis.

a. Ability of iron chelator deferoxamine (DFO) to prevent ferroptosis upon treatment with ferroptocide or positive control RSL3 for 1 hr in ES-2 cells (C11-BODIPY probe, lipid ROS). Data is representative of three independent biological experiments. **b**. Lipophilic antioxidant Trolox (250 μM) rescues ES-2 cells from ferroptocide-induced cytotoxicity after 14 hr incubation. **c**. Ability of ferroptosis inhibitor, ferrostatin (2 μM), to protect cells against ferroptocide treatment after 14 hr in ES-2 cells. **d**. Effect of DFO (100 μM) on viability of ES-2 cells after 14 hr incubation with ferroptocide and erastin (positive control). **e**. Comparison of speed of cell death of ferroptocide, RSL3, and erastin, each at 10 μM in HCT 116 and A549 (two K-RAS mutant cancer cell lines) respectively. **b–e**. Cell viability was determined with AV/PI staining. Data are plotted as the mean ± s.e.m., n=3 biological replicates. Two-sided t-test, **** $P < 0.0001$, *** $0.0001 \leq P < 0.001$, ** $0.001 \leq P < 0.01$,

n.s. $P > 0.05$ (P values were $1.1\ E^{-5}$, $1.8\ E^{-6}$, 0.0001, 0.009 for trolox; $3.3\ E^{-8}$, $6.5\ E^{-6}$, $1.7\ E^{-7}$, 0.0008, for ferrostatin-1; 0.0002, $3.3\ E^{-8}$, $4.5\ E^{-9}$, 0.003 for DFO from left to right).

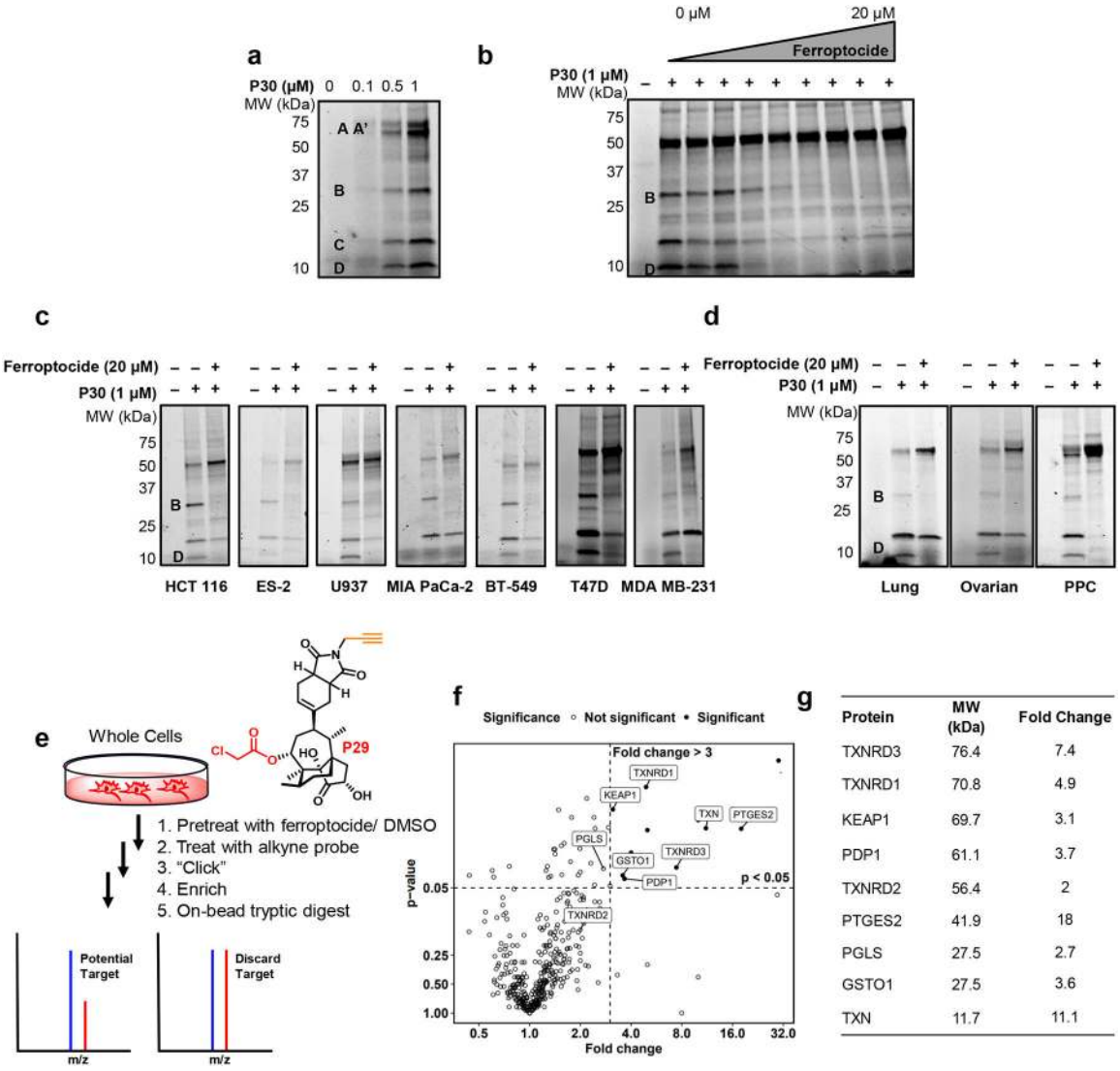

Protein	MW (kDa)	Fold Change
TXNRD3	76.4	7.4
TXNRD1	70.8	4.9
KEAP1	69.7	3.1
PDP1	61.1	3.7
TXNRD2	56.4	2
PTGES2	41.9	18
PGLS	27.5	2.7
GSTO1	27.5	3.6
TXN	11.7	11.1

Figure 5: Ferroptocide selectively and covalently modifies its target in cells.

a. Proteomic profile for fluorescent analogue **P30** in HCT 116 cells after 60 min treatment reveals labeling of five main bands, n=3 biological replicates. (Note: Band A and A' often appear as one band). Coomassie stain of gel demonstrates equal loading (Figure S9a). **b**. Competitive profiling of the proteomic reactivity of **P30** with ferroptocide. HCT 116 cells were pre-treated with DMSO or various concentrations of ferroptocide (30 min) followed by treatment with **P30** (1 μM, 30 min) and in-gel fluorescence analysis, n=3 biological replicates. Coomassie stain of gel demonstrates equal loading (Supplementary Fig. 9b). **c**. Ferroptocide covalently modifies the same target(s) in multiple cell lines. Competition experiments were performed by treatment of cells with DMSO or ferroptocide (20 μM, 30 min) followed by **P30** incubation (1 μM, 30 min) and then analyzed using an in-gel fluorescence assay. Images are representative of three biological replicates. Coomassie stain of gels demonstrates equal loading (Supplementary Fig. 9c). **d**. Ferroptocide causes the same proteomic competitive profile in primary cells isolated from metastatic cancer patient samples. These cells were pre-treated with DMSO or ferroptocide (20 μM, 30 min) followed

by **P30** incubation (1 μM, 30 min) and in-gel fluorescence analysis. Representative images of two biological replicates. PPC: primary peritoneal carcinomatosis. Coomassie stain of gels demonstrates equal loading (Supplementary Fig. 9d). **e**. Schematic of biotin-streptavidin pulldown method: Treatment of HCT 116 cells with ferroptocide (20 μM, 30 min) and **P29** (20 μM, 60 min) was followed by CuAAC reaction with biotin-azide and enrichment with streptavidin magnetic beads. On-bead trypsin digestion coupled to LC/LC–MS/MS provided a list of over 300 targets (see Data Package 2). **f**. Enrichment of proteins based on P values <0.05 and fold change >3 in HCT 116 cells, n=2 independent experiments, two-sided student t-test. Thioredoxin (TXN) was a top target candidate. **g**. Proteins identified for follow-up characterization based on shared enrichment in both HCT 116 and ES-2 cell lines, as well as molecular weights matching the bands observed by gel.

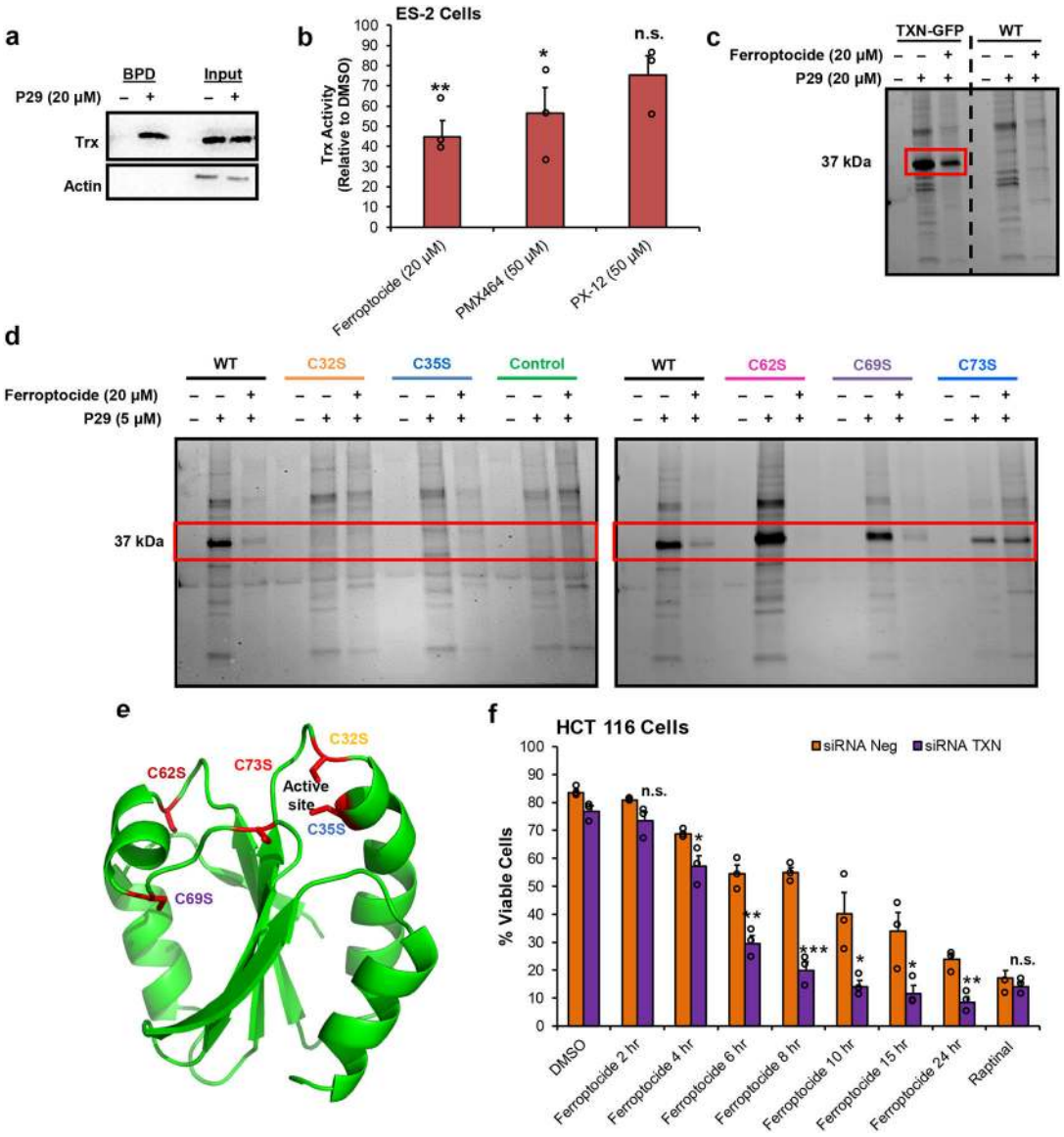

Figure 6: Ferroptocide modulates active site cysteines of thioredoxin.

a. Immunoblot of thioredoxin pulldown upon treatment of HCT 116 cells with DMSO or **P29** (20 μM, 60 min) followed by CuAAC reaction with biotin-azide and streptavidin enrichment. BPD (biotin pulldown) and input (soluble cell lysate). Images are representative of three biological experiments. **b**. Effect of ferroptocide (20 μM) and known inhibitors PMX464 and PX-12 (50 μM) on thioredoxin activity in ES-2 cells after 30 min incubation. Data are represented as mean ± s.e.m, two-sided student t-test, P-values are relative to DMSO control (0.003 and 0.03 from left to right); ** 0.001 ≤P < 0.01, * 0.01 ≤P < 0.05, n.s. P > 0.05, n=3 independent experiments. **c**. Competition profile of thioredoxin labeling by probe **P29** (20 μM, 60 min) upon pretreatment with DMSO or ferroptocide (20 μM, 30 min) followed by CuAAC with Cy3 azide in HCT 116 cells overexpressing TXN-GFP plasmid vs. non-transfected (wild type, WT) cells, Cy3 channel. Red box indicates competition of the band of interest. Representative in-gel fluorescence images of n=3

biological replicates. Coomassie stain of gel demonstrates equal loading (Supplementary Fig. 10). **d**. Identification of ferroptocide labeling sites on thioredoxin. In-gel fluorescence scanning of HCT 116 cells overexpressing each cysteine-mutated thioredoxin. Cells were pre-treated with DMSO or ferroptocide (20 μM, 30 min) followed by incubation with **P29** probe (5 μM, 60 min) and then CuAAC reaction with Cy3 azide. The serine mutations of the active site cysteines 32, 35 and cysteine 73 diminished compound labeling. Data are representative of three biological replicates. Coomassie stain of gels demonstrates equal loading (Supplementary Fig. 11). **e**. Crystal structure of thioredoxin with cysteine residues colored in red (PIB:1ERT). **f**. siRNA of thioredoxin in HCT 116 cells (48 hr) sensitizes them to ferroptocide treatment (10 μM) but not Raptinal (10 μM) at the indicated time points. Note: siRNA of TXN at 48 hr is not toxic to cells. Cell viability was determined with AV/PI staining. Data are plotted as the mean ± s.e.m., n=3 biological replicates. Two-sided student t-test, **** $P < 0.0001$, *** $0.0001 \leq P < 0.001$, ** $0.001 \leq P < 0.01$, n.s. $P > 0.05$ (P values were 0.04, 0.004, 0.0006, 0.03, 0.04, 0.006 from left to right).

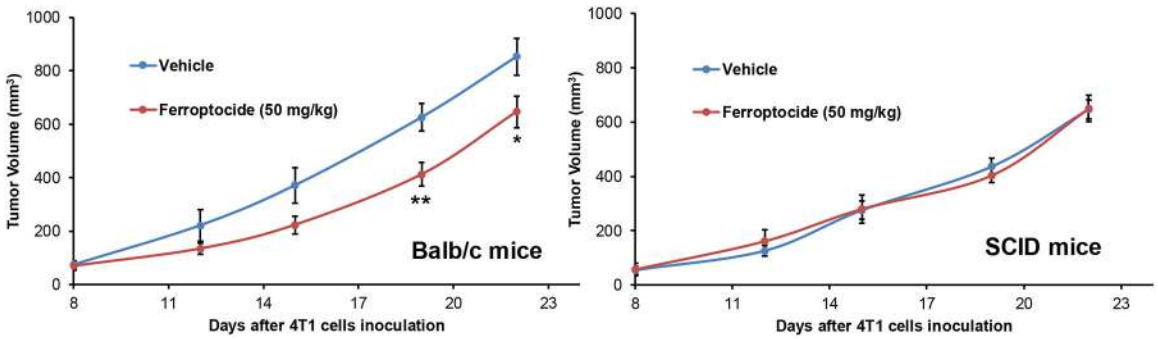

Figure 7: Ferroptocide modulates the immune system.

Ferroptocide inhibits subcutaneous 4T1 tumor growth in immunocompetent Balb/c mice (left) but not in immunodeficient SCID mice (right) as measured by tumor volume. Ferroptocide was administered intraperitoneally at 50 mg/kg, twice a week, five doses (n=7 mice per group). Data represent the mean ± s.e.m. Two-sided student t-test, P values are relative to vehicle control; ** $p < 0.01$, * $0.01 \leq p < 0.05$ (0.009 and 0.04 from left to right).